On-chip aberration correction for planar nanofocusing x-ray lenses by focused ion-beam milling

Frank Seiboth ✉ 🅿 ; Andreas Schropp 🅿 ; Mikhail Lyubomirskiy 🅿 ; Wenxin Wang 🅿 ; Andreas Jahn;
Satishkumar Kulkarni 🅿 ; Thomas F. Keller 🅿 ; Christian G. Schroer 🅿

Check for updates

View Online   Export Citation   CrossMark
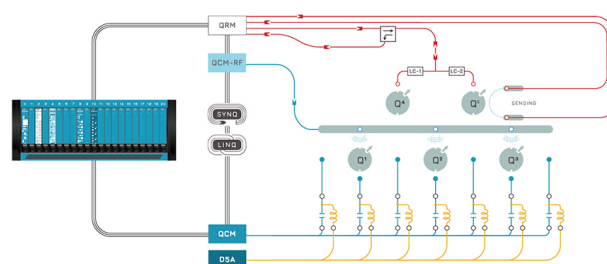
On-chip aberration correction for planar nanofocusing x-ray lenses by focused ion-beam milling

View Online   Export Citation   CrossMark

Frank Seiboth,[1,a] Andreas Schropp,[1,2] Mikhail Lyubomirskiy,[1] Wenxin Wang,[1,3] Andreas Jahn,[4]
Satishkumar Kulkarni,[1] Thomas F. Keller,[1,5] and Christian G. Schroer[1,2,5]

AFFILIATIONS

[1]Center for X-ray and Nano Science CXNS, Deutsches Elektronen-Synchrotron DESY, Notkestr. 85, 22607 Hamburg, Germany
[2]Helmholtz Imaging, Deutsches Elektronen-Synchrotron DESY, Notkestr. 85, 22607 Hamburg, Germany
[3]European X-ray Free-Electron Laser Facility, Holzkoppel 4, 22869 Schenefeld, Germany
[4]Institute of Semiconductors and Microsystems, Technische Universität Dresden, 01062 Dresden, Germany
[5]Department Physik, Universität Hamburg, Luruper Chaussee 149, 22761 Hamburg, Germany

[a]Author to whom correspondence should be addressed: frank.seiboth@desy.de

ABSTRACT

Aberration-free x-ray optics are a prerequisite for nondestructive scanning x-ray microscopy with highest spatial resolution in order to understand complex material systems and processes. Nevertheless, due to highly challenging manufacturing requirements, even state-of-the-art x-ray optics often still suffer from residual lens aberrations, and diffraction-limited performance can often only be achieved by inserting additional corrective optical elements. Here, the concept of tailor-made refractive x-ray phase plates is expanded by integrating these corrective optical elements into the focusing device directly. In this case, planar nanofocusing x-ray lenses out of silicon are corrected for aberrations by structuring the phase plate into the lens chip via focused ion-beam milling. The concept is demonstrated by focusing x-rays with an energy of 18 keV into a diffraction-limited focal spot with a size of $50 \times 65 \, \text{nm}^2$ full-width at half-maximum and a reduction in residual intensity outside the focus by a factor of well over three.

Nanofocusing refractive x-ray lenses (NFLs) are used in modern synchrotron radiation facilities to provide focal spot sizes below 100 nm for full-field imaging[1] and scanning microscopy applications with various contrasts.[2–4] There is no fundamental limit in numerical aperture (NA) for refractive optics,[5] and spot sizes of a few tens of nanometers have been achieved.[6,7] However, practical considerations for working distance and transmission typically limit the spot size. In contrast, diffractive optics can reach spot sizes below 10 nm with high efficiency,[8,9] and reflective optics have demonstrated focal spot sizes of 25 nm,[10] limited by the critical angle of total reflection.

An advantage of refractive optics is their potential to create almost perfectly clean nanobeams with a Gaussian intensity profile. Due to their parabolic thickness profile, the pupil function of refractive optics is a truncated Gaussian, in contrast to circular or rectangular apertures for diffractive and reflective optics. Since the point spread function (PSF) is given by the squared modulus of the Fourier transform of the pupil function, refractive optics create a nearly Gaussian PSF, whereas oscillating Bessel or sinc functions are created by circular and rectangular apertures. While the focus of a Gaussian pupil optic can contain a factor $\eta_{\text{Gauss}} \geq 0.98$ of the total radiation, the focus of flat pupil function optics contains $\eta_{\text{flat}} \approx 0.85$ at best. Here, we define the two-dimensional focus as the area within the first minimum of the Bessel or sinc function at a radius of 1.22 and within the same area of a Gaussian fitted for optimal approximation of the pattern with a waist radius of $\omega_0 = 0.84$. Considering the amount of background intensity spread around the central focal spot, a Gaussian focus provides a reduction by a factor of $(1 - \eta_{\text{flat}})/(1 - \eta_{\text{Gauss}}) \geq 10$. For mirror optics, an apodizing slit can also reduce side-lobes in a two-stage focusing scheme at the expense of intensity.[11] A clean measurement signal originating from the central peak of a nanofocused beam is crucial in background-sensitive experiments such as small- or wide-angle x-ray diffraction from low-contrast

samples contained in sophisticated *in situ* environments[12–14] or diamond anvil cells.[15,16]

Deep reactive ion etching techniques allow the fabrication of NFLs in silicon,[17,18] silicon carbide,[19] and diamond.[20,21] Minuscule control of the etching process is required in order to achieve a constant parabolic lens profile across the whole wafer and over the full etch depth.[22,23] Due to the combination of several tens to hundreds of single lenses, systematic etching errors on each lens surface are amplified when the x-ray beam is propagating through the lens stack. The induced aberrations increase the background intensity significantly and can lead to a focal spot that is not diffraction-limited anymore. Refractive phase plates for hard x-ray optics[24] present a solution to overcome these technological limitations with a corrective optical element made to measure. Here, we present the correction of aberrations in a crossed pair of silicon NFLs with on-chip corrective phase plates.

The NFLs contain a Si blank area of rectangular shape, depicted in Figs. 1(b), 1(d), and 1(e), which can be precisely structured in one dimension by focused ion-beam (FIB) milling in a subsequent processing step. Its size in beam direction of 50 μm was chosen such that maximum expected phase errors of the NFLs can be corrected for. The focused wavefield of the NFLs is characterized with at-wavelength metrology based on x-ray ptychography[25–27] in order to guide the design of the corrective phase plates.[28] The ptychographic imaging experiments were conducted at the PtyNAMi instrument[29] located at beamline P06 of PETRA III during two beamtimes: a first one to characterize the NFLs including the Si blank area and a second one to investigate the performance of the lenses after structuring the Si blank area by FIB milling. The latter then acts as a phase plate permanently integrated into the optics to compensate for residual aberrations of the NFL-optics.

X-rays with an energy of $E = 18$ keV were selected by a Si-111 channel-cut monochromator. Figure 1(a) shows the schematic configuration at the endstation. A pair of slits directly in front of the silicon NFLs confined the beam to the geometrical lens aperture of 20 $\times 30\ \mu$m^2 (h $\times$ v). In Table I, parameters of the vertically focusing lens (vNFL) and horizontally focusing lens (hNFL) are summarized. A sketch of the Si wafer design for a single lens row is shown in Fig. 1(b), with a more detailed view and description of lens geometry parameters in Fig. 1(c). The vNFL was mounted upstream and is followed by the hNFL. The distance between the NFL chips was adapted, such that the focal planes in the vertical and horizontal directions coincide to form a common focal spot. A pinhole with a 30 μm diameter was mounted close to the focal plane to further reduce stray radiation. The focused wavefield was characterized via ptychography by placing a Siemens star resolution test chart in the vicinity of the focal plane and recording far-field diffraction patterns on an Eiger X 4M pixel detector,[30] placed
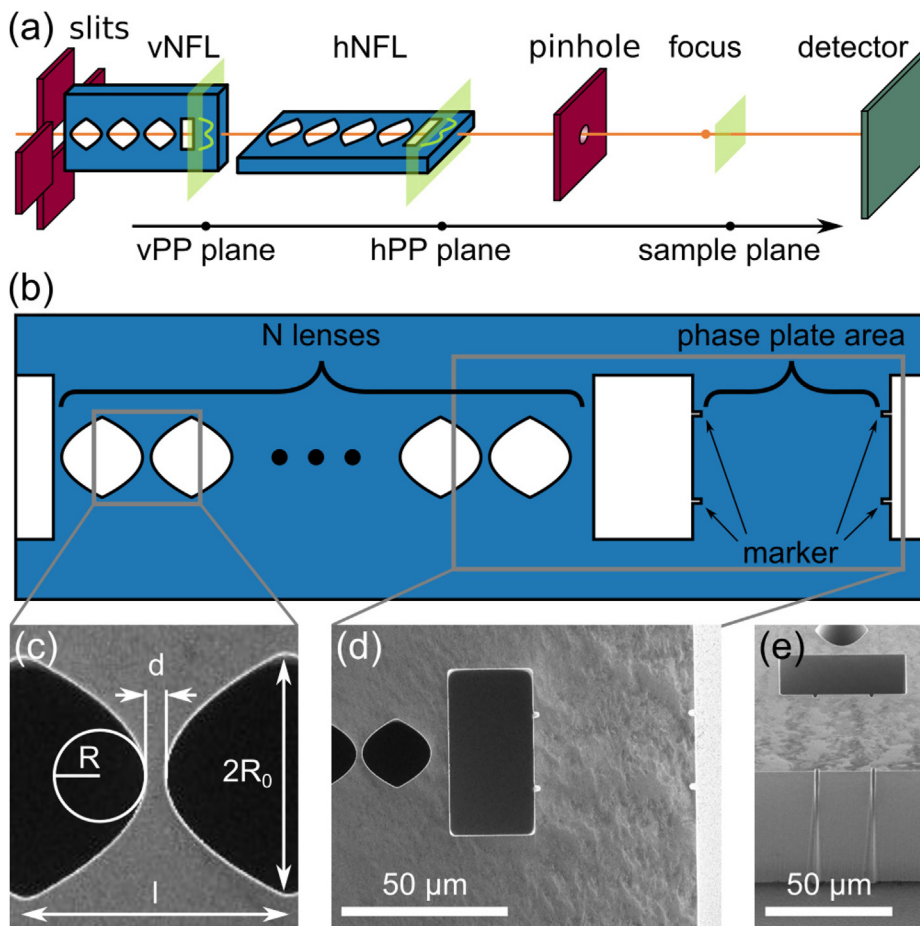
FIG. 1. Experimental configuration and the lens wafer design. (a) Sketch of the experimental setup. (b) Top view sketch showing the wafer design of a lens row on the etched Si chip. (c) Scanning electron microscopy (SEM) image of a single lens with geometry parameters. (d) SEM image of the Si blank area at the lens exit. The feature is on both the hNFL and vNFL chips in order to fabricate a phase plate for the lenses individually. (e) Tilted view SEM image of the lens exit area and markers required for an accurate positioning of the NFLs during FIB milling. The markers were etched into the Si chip together with the NFLs.

TABLE I. Parameters for the lenses at $E = 18$ keV. The geometrical parameters are described in Figs. 1(b) and 1(c).

Parameters	vNFL	hNFL
Radius of curvature R (μm)	8.086	5.278
Number N of bi-concave lenses	118	154
Web thickness d (μm)	1.5	1.5
Geometrical aperture $2R_0$ (μm)	30	20
Single lens length l (μm)	31.5	21.5
Focal length (mm)	23.37	12.07
Numerical aperture NA (10^{-4})	4.112	5.645
Diffraction limit (nm)	63	46
Transmission	0.33	0.32

3.175 m downstream of the focal plane. The sample was raster scanned in a regular grid pattern with a dwell time of 0.5 s per scan point. A square area of $6 \times 6 \, \mu m^2$ was scanned with a step size of 40 nm. After 500 iterations, we retrieved the complex-valued wavefield Ψ_{sample} created by the crossed NFL pair at the sample plane, as indicated in Fig. 1(a). Using the Fresnel-Kirchhoff diffraction formula and the theoretical values for the focal length given in Table I, the wavefield Ψ_{sample} was numerically back-propagated to the exit plane of the hNFL, yielding Ψ_{hPP}. The corresponding wavefront error, retrieved by fitting the first 4 Zernike-like polynomials for a rectangular aperture[31] to correct for tilt and defocus, is shown in Fig. 2(a). The circular Zernike polynomial basis was used to compose a new set of basis functions on a square aperture through the Gram–Schmidt orthonormalization process,[32] where the Zernike unit circle circumscribed the entire square aperture. In a second step, the wavefield was further propagated to retrieve Ψ_{vPP} at the exit of the vNFL, and its corresponding wavefront error is shown in Fig. 2(e). Here, the hNFL was simply omitted, and a

free-space propagation was performed, as we are only interested in the vertical component. For orthogonally oriented, one-dimensionally focusing lenses, the wavefield can be separated into horizontal and vertical components that do not influence each other. By averaging the phase error in the vertical direction of Ψ_{hPP} between the dashed lines highlighted in Fig. 2(a), the horizontal phase error is retrieved and plotted in blue in Fig. 2(b). The steep gradients on the edge of the wavefield likely originate from the sharp aperture slits. Assuming that the etching errors for the NFL are symmetrical to the optical axis, we subsequently fitted a symmetric height profile for the phase plate structure (hPP), shown in green in Fig. 2(b). The gradient on the outer aperture was reduced and continued to slightly beyond the geometrical aperture of the hNFL in order to avoid scattering on sharp edges within the geometric aperture of the NFLs. The same procedure was performed for the vNFL. The corresponding vertical phase-error component in blue and the derived symmetric vPP profile in green are shown in Fig. 2(f).

The phase plate structure was implemented on the NFL wafer pieces using a dual electron and focused ion-beam instrument.[33] Both calculated hPP and vPP designs were imposed into the Si blank area, shown in Figs. 1(d) and 1(e), by careful material removal using ion-beam milling with a low current of 15 nA at 30 kV. The phase plate structure was thereby milled from top to bottom of the lower edge of that blank, as shown for the hNFL and vNFL in Figs. 2(c) and 2(d) and 2(g) and 2(h), respectively. The SEM images indicate a homogeneous thickness profile with a slight widening toward the bottom of the Si wafer.

During the second beamtime, the NFLs with the now integrated corrective phase plate structures were again characterized by x-ray ptychography at PtyNAMi. This time, the detector was positioned at a distance of 3.52 m downstream of the Siemens star resolution test chart. A square area of $4 \times 4 \, \mu m^2$ was raster scanned in a regular grid pattern with a 200 nm step size and a dwell time of 0.5 s per point.
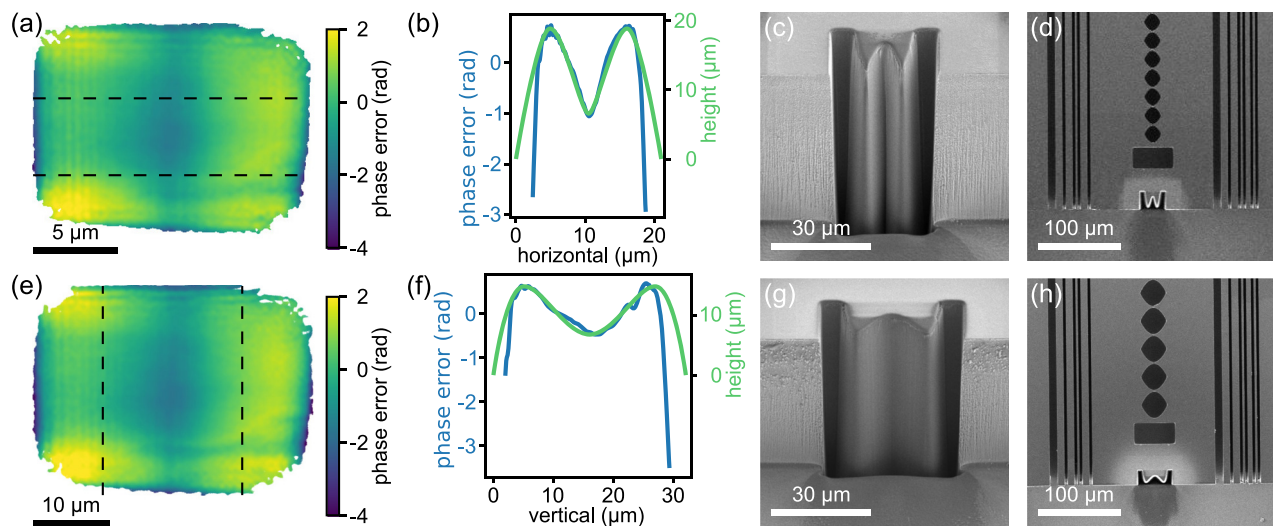

FIG. 2. Design of the on-chip phase plate. (a)–(d) Correction of hNFL. (e)–(h) Correction of vNFL. (a) and (e) Wavefront error at the exit of the hNFL and vNFL, respectively. (b) and (f) Wavefront error (blue line), derived from the area between the dashed lines in (a) and (e), respectively. The green line shows the derived phase plate height profile. (c) and (g) Tilted view SEM images of the hPP and vPP structures at the lens exit. (d) and (h) Top view SEM images of the exit area from the hNFL and vNFL with structured phase plate at the exit, shown at the bottom.

Figure 3(a) shows the previously measured wavefront error behind the uncorrected NFL pair at the exit of the hNFL [identical to Fig. 2(a), but with different color scale]. The standard deviation σ_{noPP} of the phase error is 0.75 rad. The wavefront error with implemented phase plate for both the vNFL and hNFL is shown in Fig. 3(b) for direct comparison. A reduction in wavefront error to $\sigma_{PP} = 0.32$ rad is achieved. Figure 3(c) shows a comparison of the phase error in the horizontal direction, averaged along the vertical direction. Here, the phase plate clearly leads to an improvement, reducing σ_h from 0.60 rad down to 0.18 rad. For the vertical phase error, shown in Fig. 3(d), an improvement for σ_v from 0.30 rad down to 0.14 rad is observed. The resulting impact on focal spot characteristics is highlighted in Fig. 4. The beam caustic for the uncorrected NFL pair in the horizontal and vertical directions is shown in Figs. 4(a) and 4(b), respectively. In the horizontal direction, the phase errors lead to tails on the upstream side of the focus, indicated by the arrow. In the vertical direction, the initial phase errors are on a level that barely lead to any visible aberration. For the corrected NFL pair, shown in Figs. 4(c) and 4(d) for the horizontal and vertical directions, the tails in the horizontal direction vanished, and also in the vertical direction, smaller improvements can be recognized. The uncorrected NFL pair created a focal spot of 52×68 nm^2 full-width at half-maximum (FWHM), shown in Fig. 4(e), with pronounced side-lobes especially in the horizontal direction. An improvement of the focal spot size to 50×65 nm^2 FWHM is achieved with the corrective phase plates, and horizontal sidelobe intensity is significantly reduced. The reached focal spot size agrees well with theoretical values listed in Table I. The radially averaged intensity distribution, plotted in Fig. 4(g), confirms a reduction of intensity in the first sidelobe by an order of magnitude. In return, the fraction of the total intensity that is concentrated in the central focal peak, expressed by the Strehl ratio, is improved from 0.82 to 0.95. This translates to a reduction in residual intensity outside the central focal peak by a factor of 3.6.

When dividing the maximum height of the calculated phase plate structures shown in Figs. 2(b) and 2(f) by the number of horizontal
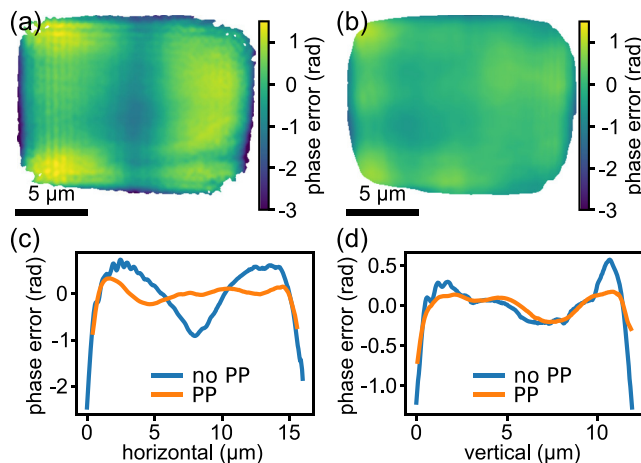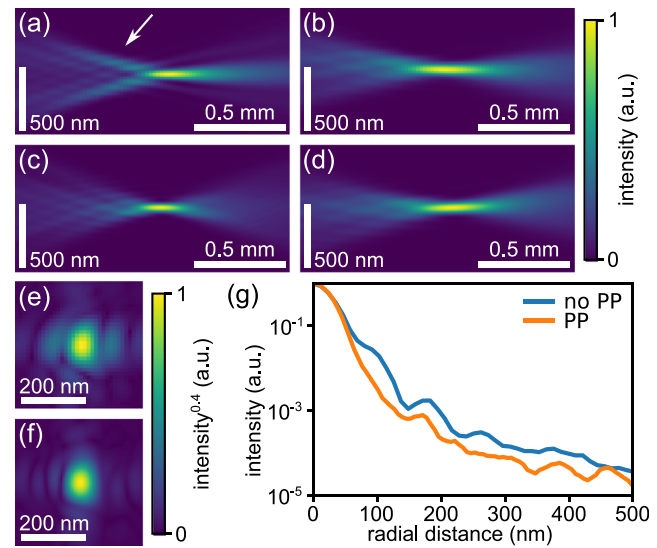
FIG. 4. Effects of aberration correction to the x-ray nanobeam. (a) and (b) Horizontal and vertical beam caustic without phase plates, respectively. (c) and (d) Horizontal and vertical beam caustic with phase plates, respectively. (e) and (f) Beam intensity in the focal plane without and with phase plates, respectively. (g) Radially averaged intensity profile in the focal plane.

and vertical lens surfaces, respectively, the maximum etching error for a single surface is $18.8\,\mu\text{m}/(2N_h) = 61$ nm for the hNFL and $14.8\,\mu\text{m}/(2N_v) = 63$ nm for the vNFL. This highlights the challenging manufacturing requirements for NFLs and emphasizes the need to integrate correction optics in a subsequent step in order to reach ultimate focusing performance. Since both the horizontally and vertically focusing NFLs were structured into a single Si wafer during the same etching process, similar etching errors are expected. In addition, the separation of horizontal and vertical phase errors is only valid for orthogonal lenses. Due to limitations in alignment accuracy, the typical angular error between the lenses is $<0.2°$. This is especially relevant for the design of the vPP structure, as the backpropagation from the hPP plane to the vPP plane omits any influence from the hNFL. Figure 3(b) shows a residual phase error after correction that is not homogeneous along the horizontal and vertical directions, indicating a more complex aberration in the lenses than the assumed etch-depth independent phase error separated into horizontal and vertical components. In order to correct these heterogeneous phase errors, the FIB structure would require to have a three-dimensional structure. Instead of only milling a cylindrical shape from the top, a height profile could be milled from the frontal area, similar to FIB milling of diamond lenses.[34] With this approach, a single phase plate at the exit of the downstream NFL chip could correct the crossed NFL pair.

In conclusion, the presented results demonstrate the feasibility of aberration correction for NFLs directly on the lens chip by means of FIB milling. The approach allows to compensate etching errors not only in the fabrication process of silicon NFLs but also for any other lens material where FIB milling is possible, e.g., silicon carbide or diamond. Since the corrective structure is integrated on the lens chip, additional technical equipment to align the phase plate is not required, and a permanent improvement of optical properties for these x-ray

FIG. 3. Comparison of the wavefront error. (a) Wavefront error at the exit of the hNFL without phase plates (noPP). (b) Wavefront error at the exit of the hNFL with phase plates (PP). (c) Wavefront error in the horizontal direction, vertically averaged. (d) Wavefront error in the vertical direction, horizontally averaged.

lenses is achieved. The approach is especially suited for NFLs and adiabatically focusing lenses[7] with high NA, where aberrations are typically larger due to the combination of many lenses and small radii of curvature R. The technique allows to further increase the performance of refractive x-ray lenses and significantly lower the noise floor of the focused Gaussian beam. This benefits experiments requiring a very clean Gaussian nanofocused x-ray beam like, e.g., diffraction studies with diamond anvil cells.[15,16] With further advances in FIB milling, also three-dimensional structures could be milled into the wafer, allowing to correct more complex and etch-depth dependent aberration.

AUTHOR DECLARATIONS

Conflict of Interest

The authors have no conflicts to disclose.

Author Contributions

Frank Seiboth: Conceptualization (equal); Data curation (lead); Formal analysis (lead); Investigation (equal); Writing – original draft (lead); Writing – review & editing (equal). **Andreas Schropp:** Conceptualization (equal); Investigation (equal); Writing – review & editing (equal). **Mikhail Lyubomirskiy:** Investigation (equal); Writing – review & editing (equal). **Wenxin Wang:** Investigation (equal); Writing – review & editing (equal). **Andreas Jahn:** Investigation (equal); Writing – review & editing (equal). **Satishkumar Kulkarni:** Formal analysis (equal); Investigation (equal); Writing – review & editing (equal). **Thomas Florian Keller:** Conceptualization (equal); Funding acquisition (equal); Supervision (equal); Writing – review & editing (equal). **Christian Gustav Schroer:** Conceptualization (equal); Funding acquisition (lead); Supervision (lead); Writing – review & editing (equal).

DATA AVAILABILITY

The data that support the findings of this study are available from the corresponding author upon reasonable request.

REFERENCES

[1] H. Simons, F. Stöhr, J. Michael-Lindhard, F. Jensen, O. Hansen, C. Detlefs, and H. F. Poulsen, Opt. Commun. **359**, 460 (2016).

[2] C. G. Schroer, P. Boye, J. M. Feldkamp, J. Patommel, A. Schropp, D. Samberg, S. Stephan, M. Burghammer, S. Schoder, C. Riekel, B. Lengeler, G. Falkenberg, G. Wellenreuther, M. Kuhlmann, R. Frahm, D. Lutzenkirchen-Hecht, and W. H. Schroeder, Acta Phys. Pol., A **117**, 357 (2010).

[3] C. Ossig, C. Strelow, J. Flügge, A. Kolditz, J. Siebels, J. Garrevoet, K. Spiers, M. Seyrich, D. Brückner, N. Pyrlik, J. Hagemann, F. Seiboth, A. Schropp, R. Carron, G. Falkenberg, A. Mews, C. G. Schroer, T. Kipp, and M. E. Stuckelberger, Materials **14**, 228 (2021).

[4] P. Villanueva-Perez, H. Fleckenstein, M. Prasciolu, K. T. Murray, M. Domaracký, K. Gregorič, V. Mariani, L. Gelisio, M. Kuhn, J. Hannappel, O. Yefanov, N. Ivanov, I. Sarrou, D. Pennicard, J. Becker, M. von Zimmermann, O. Gutowski, A.-C. Dippel, H. N. Chapman, and S. Bajt, Opt. Lett. **46**, 1920 (2021).

[5] C. G. Schroer and B. Lengeler, Phys. Rev. Lett. **94**, 054802 (2005).

[6] C. G. Schroer, O. Kurapova, J. Patommel, P. Boye, J. Feldkamp, B. Lengeler, M. Burghammer, C. Riekel, L. Vincze, A. van der Hart, and M. Kuchler, Appl. Phys. Lett. **87**, 124103 (2005).

[7] J. Patommel, S. Klare, R. Hoppe, S. Ritter, D. Samberg, F. Wittwer, A. Jahn, K. Richter, C. Wenzel, J. W. Bartha, M. Scholz, F. Seiboth, U. Boesenberg, G. Falkenberg, and C. G. Schroer, Appl. Phys. Lett. **110**, 101103 (2017).

[8] H. Mimura, S. Handa, T. Kimura, H. Yumoto, D. Yamakawa, H. Yokoyama, S. Matsuyama, K. Inagaki, K. Yamamura, Y. Sano, K. Tamasaku, Y. Nishino, M. Yabashi, T. Ishikawa, and K. Yamauchi, Nat. Phys. **6**, 122 (2010).

[9] S. Bajt, M. Prasciolu, H. Fleckenstein, M. Domaracký, H. N. Chapman, A. J. Morgan, O. Yefanov, M. Messerschmidt, Y. Du, K. T. Murray, V. Mariani, M. Kuhn, S. Aplin, K. Pande, P. Villanueva-Perez, K. Stachnik, J. P. Chen, A. Andrejczuk, A. Meents, A. Burkhardt, D. Pennicard, X. Huang, H. Yan, E. Nazaretski, Y. S. Chu, and C. E. Hamm, Light **7**, 17162 (2017).

[10] H. Mimura, H. Yumoto, S. Matsuyama, Y. Sano, K. Yamamura, Y. Mori, M. Yabashi, Y. Nishino, K. Tamasaku, T. Ishikawa, and K. Yamauchi, Appl. Phys. Lett. **90**, 051903 (2007).

[11] K. P. Khakurel, T. Kimura, H. Nakamori, T. Goto, S. Matsuyama, T. Sasaki, M. Takei, Y. Kohmura, T. Ishikawa, K. Yamauchi, and Y. Nishino, J. Synchrotron Radiat. **24**, 142 (2017).

[12] Y. Fam, T. L. Sheppard, J. Becker, D. Scherhaufer, H. Lambach, S. Kulkarni, T. F. Keller, A. Wittstock, F. Wittwer, M. Seyrich, D. Brueckner, M. Kahnt, X. Yang, A. Schropp, A. Stierle, C. G. Schroer, and J.-D. Grunwaldt, J. Synchrotron Rad. **26**, 1769 (2019).

[13] S. Weber, D. Batey, S. Cipiccia, M. Stehle, K. L. Abel, R. Gläser, and T. L. Sheppard, Angew. Chem., Int. Ed. **60**(40), 21772–21777 (2021).

[14] S. Das, R. Pashminehazar, S. Sharma, S. Weber, and T. L. Sheppard, Chem. Inge. Tech. **94**, 1591 (2022).

[15] K. Glazyrin, S. Khandarkhaeva, T. Fedotenko, W. Dong, D. Laniel, F. Seiboth, A. Schropp, J. Garrevoet, D. Brückner, G. Falkenberg, A. Kubec, C. David, M. Wendt, S. Wenz, L. Dubrovinsky, N. Dubrovinskaia, and H.-P. Liermann, J. Synchrotron Radiat. **29**, 654 (2022).

[16] W. Dong, K. Glazyrin, S. Khandarkhaeva, T. Fedotenko, J. Bednarčík, E. Greenberg, L. Dubrovinsky, N. Dubrovinskaia, and H.-P. Liermann, J. Synchrotron Radiat. **29**, 1167 (2022).

[17] V. Aristov, M. Grigoriev, S. Kuznetsov, L. Shabelnikov, V. Yunkin, T. Weitkamp, C. Rau, I. Snigireva, A. Snigirev, M. Hoffmann, and E. Voges, Appl. Phys. Lett. **77**, 4058 (2000).

[18] C. G. Schroer, M. Kuhlmann, U. T. Hunger, T. F. Gunzler, O. Kurapova, S. Feste, F. Frehse, B. Lengeler, M. Drakopoulos, A. Somogyi, A. S. Simionovici, A. Snigirev, I. Snigireva, C. Schug, and W. H. Schroder, Appl. Phys. Lett. **82**, 1485 (2003).

[19] M. Lyubomirskiy, B. Schurink, I. A. Makhotkin, D. Brueckner, F. Wittwer, M. Kahnt, M. Seyrich, F. Seiboth, F. Bijkerk, and C. G. Schroer, Opt. Express **29**, 14025 (2021).

[20] O. J. L. Fox, L. Alianelli, A. M. Malik, I. Pape, P. W. May, and K. J. S. Sawhney, Opt. Express **22**, 7657 (2014).

[21] M. Lyubomirskiy, P. Boye, J. M. Feldkamp, J. Patommel, S. Schoeder, A. Schropp, M. Burghammer, C. Wild, and C. G. Schroer, J. Synchrotron Radiat. **26**, 1554 (2019).

[22] F. Stöhr, J. Wright, H. Simons, J. Michael-Lindhard, J. Hübner, F. Jensen, O. Hansen, and H. F. Poulsen, J. Micromech. Microeng. **25**, 125013 (2015).

[23] F. Stöhr, J. Michael-Lindhard, J. Hübner, F. Jensen, H. Simons, A. C. Jakobsen, H. F. Poulsen, and O. Hansen, J. Vac. Sci. Technol. B **33**, 062001 (2015).

[24] F. Seiboth, A. Schropp, M. Scholz, F. Wittwer, C. Rödel, M. Wünsche, T. Ullsperger, S. Nolte, J. Rahomäki, K. Parfeniukas, S. Giakoumidis, U. Vogt,

U. Wagner, C. Rau, U. Boesenberg, J. Garrevoet, G. Falkenberg, E. C. Galtier, H. J. Lee, B. Nagler, and C. G. Schroer, Nat. Commun. **8**, 14623 (2017).

[25]A. Schropp, P. Boye, J. M. Feldkamp, R. Hoppe, J. Patommel, D. Samberg, S. Stephan, K. Giewekemeyer, R. N. Wilke, T. Salditt, J. Gulden, A. P. Mancuso, I. A. Vartanyants, E. Weckert, S. Schöder, M. Burghammer, and C. G. Schroer, Appl. Phys. Lett. **96**, 091102 (2010).

[26]F. Seiboth, M. Kahnt, M. Scholz, M. Seyrich, F. Wittwer, J. Garrevoet, G. Falkenberg, A. Schropp, and C. G. Schroer, Proc. SPIE **9963**, 99630P (2016).

[27]F. Pfeiffer, Nat. Photonics **12**, 9 (2018).

[28]F. Seiboth, F. Wittwer, M. Scholz, M. Kahnt, M. Seyrich, A. Schropp, U. Wagner, C. Rau, J. Garrevoet, G. Falkenberg, and C. G. Schroer, J. Synchrotron Radiat. **25**, 108 (2018).

[29]A. Schropp, R. Döhrmann, S. Botta, D. Brückner, M. Kahnt, M. Lyubomirskiy, C. Ossig, M. Scholz, M. Seyrich, M. E. Stuckelberger, P. Wiljes, F. Wittwer, J. Garrevoet, G. Falkenberg, Y. Fam, T. L. Sheppard, J.-D. Grunwaldt, and C. G. Schroer, J. Appl. Crystallogr. **53**, 957 (2020).

[30]I. Johnson, A. Bergamaschi, H. Billich, S. Cartier, R. Dinapoli, D. Greiffenberg, M. Guizar-Sicairos, B. Henrich, J. Jungmann, D. Mezza, A. Mozzanica, B. Schmitt, X. Shi, and G. Tinti, J. Instrumentation **9**, C05032 (2014).

[31]V. N. Mahajan, Appl. Opt. **49**, 6924 (2010).

[32]W. Swantner and W. W. Chow, Appl. Opt. **33**, 1832 (1994).

[33]A. Stierle, T. F. Keller, H. Noei, V. Vonk, and R. Roehlsberger, J. Large-Scale Res. Facil. **2**, A76 (2016).

[34]P. Medvedskaya, I. Lyatun, S. Shevyrtalov, M. Polikarpov, I. Snigireva, V. Yunkin, and A. Snigirev, Opt. Express **28**, 4773 (2020).